# Exploration of Coincidence Detection of Cascade Photons to Enhance Preclinical Multi-Radionuclide SPECT Imaging

Yifei Jin and Ling-Jian Meng, *Member, IEEE*

*Abstract*—We proposed a technique of coincidence detection of cascade photons (CDCP) to enhance preclinical SPECT imaging of therapeutic radionuclides emitting cascade photons, such as Lu-177, Ac-225, Ra-223, and In-111. We have carried out experimental studies to evaluate the proposed CDCP-SPECT imaging of low-activity radionuclides using a prototype coincidence detection system constructed with large-volume cadmium zinc telluride (CZT) imaging spectrometers and a pinhole collimator. With In-111 in experimental studies, the CDCP technique allows us to improve the signal-to-contamination in the projection (Projection-SCR) by ~53 times and reduce ~98% of the normalized contamination. Compared to traditional scatter correction, which achieves a Projection-SCR of 1.00, our CDCP method boosts it to 15.91, showing enhanced efficacy in reducing down-scattered contamination, especially at lower activities. The reconstructed images of a line source demonstrated the dramatic enhancement of the image quality with CDCP-SPECT compared to conventional and triple-energy-window-corrected SPECT data acquisition. We also introduced artificial energy blurring and Monte Carlo simulation to quantify the impact of detector performance, especially its energy resolution and timing resolution, on the enhancement through the CDCP technique. We have further demonstrated the benefits of the CDCP technique with simulation studies, which shows the potential of improving the signal-to-contamination ratio by 300 times with Ac-225, which emits cascade photons with a decay constant of ~0.1 ns. These results have demonstrated the potential of CDCP-enhanced SPECT for imaging a super-low level of therapeutic radionuclides in small animals.

*Index Terms*—Cascade photons, scatter and crosstalk contamination, coincidence detection, SPECT imaging.

Fig. 1. An illustration of signals detected by the imaging detectors in a SPECT system.

## I. INTRODUCTION

MOLECULAR imaging technologies, i.e., single photon emission computed tomography (SPECT) and positron emission tomography (PET), play an important role in diagnosis and therapy. They could visualize the distribution of the therapeutic radionuclides emitting gamma-rays for locating the lesions, tracking the radiopharmaceuticals and determining the uptake [1], [2], [3], [4]. There is increasing interest in radiopharmaceutical therapy (RPT) and simultaneous multi-tracer SPECT imaging in recent years. In these applications, gamma-rays across a wide energy range (60-700 keV) are emitted. In the presence of multi-energy gamma-rays like Ac-225 and In-111/Tc-99m or Ga-68/Lu-177 dual-tracers, down-scattering and crosstalk could significantly degrade the image quality of SPECT imaging [5], [6], [7]. As illustrated in Fig. 1, in SPECT, signals detected for imaging by the imaging detectors could have four sources:

1) (a) Primary gamma-photons (b) going through the collimator, (c) reaching the detector with its original energy, (d) being detected inside the primary energy window.

2) (a) Primary gamma-photons, (b) penetrating the object and the aperture without any interactions, (c) being detected inside the primary energy window.

3) (a) High-energy gamma-photons, (b) not interacting with any material, or scattering in the object, and/or aperture, and/or other surrounding materials, and then (c) being detected inside the primary energy window.

4) (a) Gamma-photons with energy close to the primary energy, (b) going through or penetrating the collimator, (c) being detected inside the primary energy window.

Primary gamma-photons represent the gamma-photons to be imaged and the primary energy window is to select these primary gamma-photons. Only 1) is true signals while 2), 3) and 4) would contaminate the final image. By appropriate design of collimator, 2) can be almost eliminated. However, 3) (down-scattered contamination) and 4) (crosstalk) could overwhelm the true signals. These lead to severe degradation of the resultant image quality and affect the precision and accuracy of diagnostic results.

Over the years, numerous correction methods have been proposed to mitigate these issues. Energy window-based correction methods like dual/triple/multiple energy window correction use several energy windows to estimate the scatter imaging and are widely applied [5], [8], [9], [10], [11], [12]. There are other correction methods based on spectral analysis, including spectra fitting to split the primary photopeak and achieve high accuracy [13], [14], [15]. There are also studies on modeling the scatter and crosstalk based on, i.e., Klein–Nishina formula and Monte Carlo simulation, then using analytical methods and statistical reconstruction to estimate the contamination [16], [17], [18], [19], [20], [21], [22]. While these advanced scatter correction methods offer improved accuracy based on sophisticated models, they face challenges in complex systems. These models often become overly complicated and necessitate additional efforts for attenuation correction. Time-consuming is also one of the limitations. Recently, with increasing interest in artificial intelligence, deep-learning-based scatter correction methods have been developed [23], [24], but their robustness still remains to be improved. To apply those scatter correction methods, a large number of events are used to estimate scattering. However, in imaging of therapeutic radionuclides, even with high administered activities, the radioactive uptake in tissues of interest could be *low*, i.e., below 10 $\mu$Ci [25], [26]. In preclinical targeted-$\alpha$-therapy, the administered activity is even *super-low* (below 1 $\mu$Ci) when doing in vivo imaging of Ac-225 [27]. Due to the small number of measured events, there are few counts for spectral analysis or other compensation. Hence, the statistical fluctuation of those methods would be large. In this case, the precision and accuracy of traditional correction methods would be significantly degraded [28]. In addition, there have been several studies on using double-photon coincidence to reject crosstalk and achieve reconstruction-free imaging [29], [30], [31]. They utilized parallel hole and slit-pinhole collimators to determine the directions of double cascade photons and, in turn, to compute the positions of the emissions. Although parallel hole or slit-pinhole collimators were applied to improve the chance of detecting cascade photons, they still suffer from a problem of low sensitivity to detect double-collimated photons in coincidence.

In this study, we proposed the coincidence detection of cascade photons (CDCP) technique to dramatically reject the down-scattered and crosstalk contamination fundamentally for imaging low-activity therapeutic radionuclides. It utilizes cascade photons which refer to two or more photons emitted through an intermediate energy level. In the decay process of some important therapeutic radionuclides, such as In-111 and Lu-177, there are such cascade emissions with relatively short half-lives of the intermediate energy levels and can be considered to have strong correlations. In our proposed technique, we perform SPECT imaging on the primary gamma-photons through an aperture and use the secondary gamma-photons as a coincidence gate, which allows us to significantly reduce the down-scattered contamination and crosstalk to the primary gamma-photons. Meanwhile, the sensitivity is comparable to conventional SPECT imaging with extensive coincidence detector coverage, which enables a high detection efficiency to secondary gamma-photons.

One of the significant implications of low-activity or super-low-activity therapeutic radionuclide imaging is in vivo imaging of Ac-225 in targeted-$\alpha$-therapy, where traditional scatter correction methods work ineffectively. With the implementation of our CDCP technique, we are able to almost eliminate the substantial down-scattered and crosstalk contamination at 117 keV. Consequently, we can generate resultant images with exceptional signal-to-contamination ratios and accurately track Tl-209/Bi-213.

The main objective of this study is to experimentally demonstrate and evaluate the performance of the proposed CDCP technique. In this paper, *first*, we introduced the candidate therapeutic radionuclides and principles for the CDCP technique. Second, we constructed a prototype CDCP-SPECT system as a proof-of-principle with a pinhole collimator and large-volume CZT imaging spectrometers that offer an excellent energy resolution, i.e., 3 keV full-width-at-half-maximum (FWHM) at 200 keV, and a sub-0.5 mm FWHM intrinsic spatial resolution in 3 dimensions. *Third*, we used Ac-225 and In-111 sources to carry out some phantom studies to experimentally evaluate the effect of rejecting down-scattered contamination with the CDCP technique. Maximum-likelihood expectation-maximization algorithm was used for reconstruction. *Fourth*, we compared the effect of CDCP with a traditional scatter correction method in super-low-activity cases. *Fifth*, we used artificial energy blurring to evaluate the effect of the spectral resolution on the CDCP technique. *Finally*, to assess the impact of temporal resolution on CDCP, we derived the principles based on specific assumptions and conducted Monte Carlo simulations to validate our findings. These results provide important references to the development of preclinical CDCP-SPECT systems for imaging low-activity therapeutic radionuclides emitting cascade photons, such as Ac-225, Ra-223, Lu-177, and In-111.

## II. Materials and Methods

### A. Candidates of Therapeutic Radionuclides Emitting Cascade Photons

The criteria for selecting candidates of CDCP-SPECT are that (a) nuclides emit cascade photons, (b) the half-life of intermediate energy level should be short enough, and (c) the probability of detecting the pair of cascade photons in
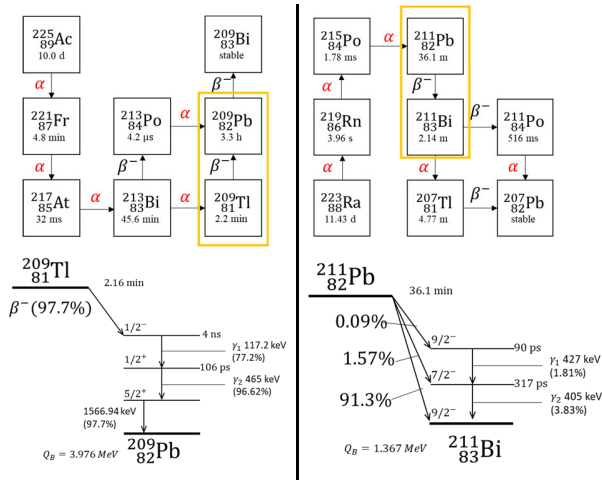
Fig. 2. (left) Decay scheme of Tl-209 in the decay chain of Ac-225, and (right) decay scheme of Pb-211in the decay chain of Ra-223.

TABLE I
PROPERTIES OF FOUR RADIONUCLIDES
EMITTING CASCADE PHOTONS

| Radionuclide (Daughter) | $\gamma_1$ | $\gamma_2$ | $T_{1/2}$ | $p(\gamma_1|\gamma_2)$ | $p(\gamma_2|\gamma_1)$ | $p(\gamma_1,\gamma_2)$ |
|---|---|---|---|---|---|---|
| Ac-225 (Tl-209) | 117 keV | 465 keV | 106 ps | 80.0% | ~100% | 1.5% |
| Ra-223 (Pb-211) | 427 keV | 405 keV | 317 ps | 45% | 95.8% | 1.7% |
| Lu-177 | 208 keV | 113 keV | 506 ps | 53.3% | 31.8% | 3.4% |
| In-111 | 171 keV | 245 keV | 84.5 ns | 96% | ~100% | 91% |

coincidence is high to obtain reasonable sensitivity. Previous research has reported that In-111 and Lu-177 have usable pairs of cascade photons [30], [31]. There are some other therapeutic radionuclides, such as Ac-225 and Ra-223, that also emit cascade photons, as shown in Fig. 2. To avoid distraction, we only show the related excited levels in the figure. The decay of Tl-209 (a daughter of Ac-225) produces a pair of cascade gamma-photons at 117 keV and 465 keV characterized by a decay constant of 106 ps. Similarly, Ra-223 decay also leads to a cascade of 405 keV and 427 keV gamma-photons from its daughter Pb-211 with a decay constant of 317 ps.

In Table I, we summarized information of some common therapeutic radionuclides in RPT, including Ac-225, Ra-223, Lu-177 and In-111.

In this table, $\gamma_1$ is emitted before $\gamma_2$. Assuming that the detection sensitivity is 100%, $p(\gamma_1|\gamma_2)$ denotes the conditional probability of detecting $\gamma_1$ given that $\gamma_2$ is detected, which satisfies

$$p(\gamma_1, \gamma_2) = p(\gamma_1|\gamma_2)\, p(\gamma_2) = p(\gamma_2|\gamma_1)\, p(\gamma_1). \quad (1)$$

In Eq. (1), $p(\gamma_2)$ is the probability of detecting $\gamma_2$ for one decay of the mother radionuclide, which is the branching ratio. $p(\gamma_1, \gamma_2)$ is the probability of detecting $\gamma_1$ and $\gamma_2$ in coincidence for one decay of the mother radionuclide. To estimate the conditional probabilities, we denote $p_{in}$ as the total probability of a mother nucleus reaching the intermediate energy level, which is the sum of the branch ratios of all processes reaching the state. Then $p(\gamma_1|\gamma_2)$ and $p(\gamma_2|\gamma_1)$
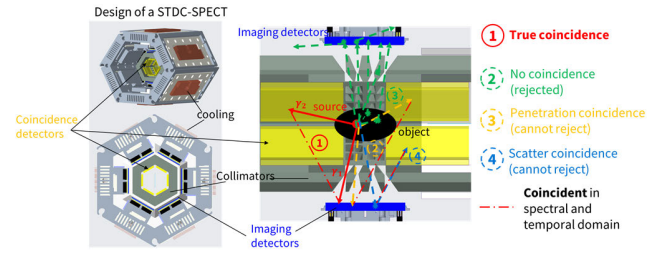


Fig. 3. (A) Schematic diagram of the proposed CDCP-SPECT system (yellow blocks are coincidence detectors), (B) illustration of CDCP-SPECT concept: Label ① shows a pair of true coincidence event (true signal) in which $\gamma_1$ goes through the pinhole and is detected in coincidence with $\gamma_2$; Label ② shows down-scattering high-energy photons (contamination), they can fall into the primary energy window as shown by these green dashed arrows, but they will be rejected because there is no coincidence for them. There is also a very small fraction of contamination contributed by penetration (label ③), scatter (label ④), and random coincidence.

can be derived as

$$p(\gamma_1|\gamma_2) = \frac{p(\gamma_1)}{p_{in}},\; p(\gamma_2|\gamma_1) = \frac{p(\gamma_2)}{p_{in}}. \quad (2)$$

In the decay chain of Ac-225, the branching ratio from Bi-213 to Tl-209 is 2%. Hence, referring to Ac-225, the branching ratio of emitting $\gamma_1$ is 1.5%, so even if $p(\gamma_2|\gamma_1)$ is nearly 100%, the total probability $p(\gamma_1, \gamma_2)$ is still low.

### B. The Principle of CDCP-SPECT

The idea of CDCP is to use a detection system that can detect the cascade gamma-photons in coincidence and, at the same time, precisely determine the energy of both gamma-photons, then we can identify the exact emission almost completely free from interference of other contamination.

For CDCP-enhanced SPECT (CDCP-SPECT), we detect the primary gamma-photons with imaging detectors. And coincidence detectors are used to detect the secondary gamma-photons. Note that we can treat $\gamma_1$ or $\gamma_2$ as the primary gamma-photon and treat the other as the secondary gamma-photon. Then temporal coincidence is applied between the interactions inside the primary energy window of imaging detectors and those inside the secondary energy window of coincidence detectors. As illustrated in Fig. 3, most of the events originating from high-energy gamma-photons are rejected because of no coincidence. Only a small fraction of contamination from penetration (label ③), scatter (label ④), and random coincidence could contaminate the reconstruction. Therefore, the CDCP technique would allow us to precisely identify primary gamma-photons with a high level of confidence and subsequently reconstruct them with SPECT imaging almost free from scattered and crosstalk contamination. Fig.3 (A) shows a designed preclinical CDCP-SPECT. In this system, imaging detectors need to have excellent spatial, energy, and timing resolutions, which could be realized with, for example, CZT. The coincidence detectors for recording the energy and timing information of the secondary gamma-photons can be made with low-cost scintillators..

When processing coincidence detection, given a radionuclide emitting $\gamma_1$ and $\gamma_2$ cascade gamma-photons, we take
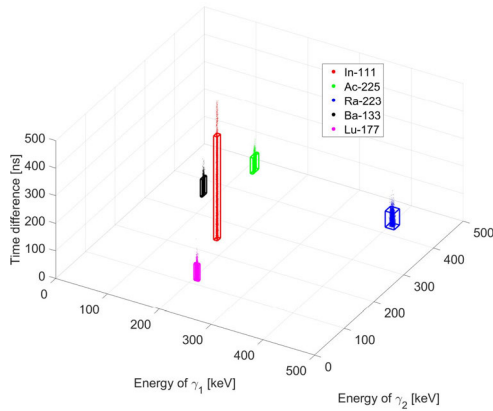
Fig. 4.  $E_1$-$E_2$-$\Delta T$ 3-dimensional windows for selecting cascade photon emission events from In-111, Ac-225, Ra-223, Ba-133, and Lu-177 in energy and time domains.



Fig. 5.  Overview of the prototype CDCP-SPECT system with CZT detectors and a pinhole collimator.

$\gamma_1$ as the primary gamma-photon and $\gamma_2$ as the secondary gamma-photon without loss of generality. The method is to go through each interaction detected by coincidence detectors with energy deposition within $\gamma_2$ energy window and open a time gate *covering* the interaction to search for interactions detected by imaging detectors. Only those interactions with the energy deposition in $\gamma_1$ energy window are considered in regular SPECT imaging. Noting that in practical use, it is better to go through all $\gamma_1$ interactions and look for $\gamma_2$ in the time gate for computation efficiency, but in this study, we did the opposite because we also aimed to estimate the spectra in coincidence with $\gamma_2$. Fig. 4 shows the true coincidence events of cascade photons emitted from different radionuclides in spectral and temporal domains, where the cubes represent the time and energy windows of CDCP. Events falling outside the boxes are rejected.

Note that CDCP cannot completely reject high-energy gamma-photons or crosstalk signals because they can still be accepted if they happen to be detected inside the $\gamma_1$ energy window and inside the time gate of a secondary gamma-photon. Such an event is defined as a random coincidence event. Similarly, a primary gamma-photon can also be rejected if its detected timestamp is not inside the time gate of the secondary gamma-photons, or the secondary gamma-photons is not detected. Given the half-life of the intermediate energy level and the timing resolution of the detection system, there is a trade-off between the number of true coincidence events and the fraction true coincidence when we select the time gate.

## C. A Prototype CDCP-SPECT System With 3-D CZT Detectors

To demonstrate the feasibility and evaluate the performance of SPECT imaging through CDCP detection, we have constructed a prototype CDCP-SPECT system with four (2×2) high-resolution 3-D position-sensitive CZT detector panels. One of the detector panels is coupled to a tungsten pinhole collimator with a diameter of 0.5 mm and thickness of 6 mm, which works as the imaging detector. The distance between the pinhole and the front surface of the coupled detector panel is 20 mm. The other three detector panels are completely open for detecting the secondary gamma-photons in coincidence,
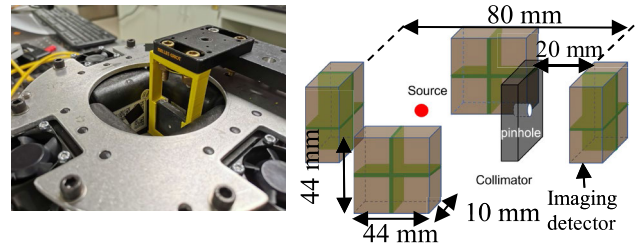
as shown in Fig. 5. The distance between the front surfaces of two opposite CZT panels is 80 mm. In this system, the sensitivity to primary gamma-photons is $s_1 =\sim 0.001\%$, while the sensitivity to secondary gamma-photons is $s_2 =\sim 3\%$. A high-resolution rotation stage and a plastic holder were used to hold the source. The rotation stage allowed the source to be rotated in order to achieve enough angular sampling.

Each CZT detector panel consists of four modules while each module is made up of a monolithic CZT crystal of $2.2 \times 2.2 \times 1.0$ cm$^3$ in size. The CZT detector module has $11 \times 11$ anode pixels with a pixel pitch of 1.9mm and a large flat panel cathode. The unique design of the detector allows it to offer an excellent energy resolution (3 keV at 200 keV, 4.5 keV at 450 keV, 5.4 keV at 511 keV). It combines cathode-to-anode ratio and electron drifting time inside the detector to provide the depth-of-interaction (DOI) information and utilize transient signals on adjacent anode pixels to achieve sub-0.5 mm intrinsic spatial resolutions in three dimensions [32], [33], [34], [35]. Noting that the positioning of interactions near the crystal boundaries is poor, we directly removed interactions on those pixels and used smaller virtual pixels of 0.2 mm pitch combining all DOI layers. Additionally, the positioning near the actual pixel edges is not smooth, so the 1.9 mm pixels can be observed from the projection. In the final image reconstruction, we artificially blurred projections with a 2-D 1.4 mm FWHM Gaussian filter. The CZT detectors work in coincidence, and the output energy, position, and time information are saved in list mode. The coincidence pairs will be determined in post-processing as described in Sec. II-B. We have previously reported that we could achieve approximately 10 ns timing resolution for large-volume CZT detectors both theoretically and experimentally [36], [37]. However, the readout circuits in this prototype system do not allow us to implement timing correction. Consequently, the coincidence timing resolution of the system is over 100 ns. The time gate used in this study is [-250 ns, 250 ns] (initiated 250 ns before the secondary gamma-photon and ended 250 ns after it).

## D. Phantom Study

Using the prototype CDCP-SPECT, we carried out two phantom studies with an Ac-225 line source and an In-111 line source fabricated with a capillary tube of 0.75 mm inner diameter.

We carried out the spectral analysis with Ac-225 to demonstrate the enhancement with the CDCP technique. However, due to the limited sensitivity ($\sim 0.3\%$) of our
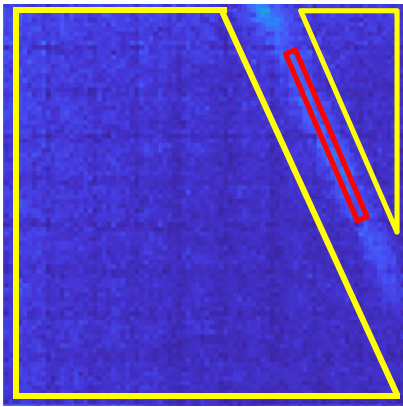
Fig. 6. Projection of an In-111 line source. The red box shows the ROI 1 while the yellow regions show the ROI 2.

prototype system to detect the secondary 465 gamma-photons from Tl-209 (one of the daughters of Ac-225), we were not able to conduct projection and imaging studies solely on Ac-225.

To demonstrate the technique comprehensively, we used an In-111 line source to conduct two studies:

1) 1.5 $\mu$Ci pure In-111 line source without any background, 2) 0.7 $\mu$Ci In-111 line source with a 0.5 $\mu$Ci Ac-225 background. In-111 was used as the source of cascade photons, thereby substituting for Tl-209, while Ac-225 provides other high-energy gamma-photons.

For both studies, we collected three angles of data at an interval of 30° for imaging. Considering the decay of In-111 during acquisition, in 1), the activities of In-111 at three angles were 1.5 $\mu$Ci, 1.3 $\mu$Ci, and 1.1 $\mu$Ci while the acquisition time for each angle was 12 hours, 13.7 hours and 15.8 hours. In 2), the activities of In-111 at three angles were 0.7 $\mu$Ci, 0.55 $\mu$Ci, and 0.35 $\mu$Ci while the acquisition time for each angle was 24 hours, 32 hours, and 50 hours. Since In-111 emits 171 keV and 245 keV photons in cascade, by taking a) 171 keV as the primary gamma-photon (245 keV as the secondary gamma-photon) and b) 245 keV as the primary gamma-photon (171 keV as the secondary gamma-photon), we did quantitative spectral, projection analysis and image reconstruction on both In-111 studies.

### E. Metrics to Estimate the Quality of Data

To estimate the quality of acquired list-mode data, we used three quantities: (a) signal-to-contamination ratio (Spectral-SCR) and (b) normalized contamination level in the *spectral* domain to estimate the number of primary and down-scattered photons, and (c) SCR in *projection* domain (Projection-SCR) to indicate the quality of projections. In the projection on the imaging detector, we selected the inner region of the projected In-111 line source as a region-of-interest (ROI 1), and the region outside the projected line source as ROI 2 as illustrated in Fig. 6. Since the object is simple, it is easy to recognize the projection of the line source through the pinhole collimator, and based on which, to define the inner (red) and outer (yellow) regions. The edges of the projected line source were not included. With a pixel pitch of 0.2 mm, the number of

pixels in ROI 1 and ROI 2 are ∼250 and ∼10,000, respectively, for 3 acquired angles.

The calculation of Spectral-SCR is based on the spectra in ROI 1. To get the spectra with CDCP, we counted all interactions falling inside the time gate covering the secondary gamma-photons in each ROI. In this region, the detector receives true primary gamma-photons through the pinhole, penetration, and down-scattered gamma-photons (signal source types 1, 2 and 3) as described in Sec. I). Since true primary gamma-photons can also be rejected by CDCP as described in Sec. II-B, we use the ratio of signal to contamination (down-scattered and crosstalk photons) to quantify the data quality in ROI 1. The calculation of the normalized contamination is based on the spectra in ROI 2. In this region, the detector does not receive the true primary gamma-photons directly going through the pinholes. Hence, we only estimated the contamination level. The calculation of the Projection-SCR is based on the whole projection. Again, since the whole projection contains true primary gamma-photons, which can be reduced by CDCP, we use Projection-SCR to show the projection quality.

To calculate the Spectral-SCR in ROI 1, we fitted the contamination curve around the primary gamma energy $E_1$ with 1-dimensional polynomial fitting and used Gaussian fitting to fit the primary gamma peak after subtracting the fitted contamination curve. The standard deviation $\sigma_1$ from the Gaussian fitting was used to set the primary energy window of $E_1 \pm 3\sigma_1$ for the following computation. Based on the fitted contamination curve, we can compute the contamination and the net area of the peak within the primary energy window as *contamination* and *signal* to calculate Spectral-SCR

$$\text{Spectral} - \text{SCR} = \frac{signal}{contamination}. \tag{3}$$

In ROI 2, only the contamination curve within the energy window was integrated. Given that the total counts, acquisition time, and the area of ROI 2 were different for different acquisitions, the absolute values of contamination could not be compared directly. Therefore, we normalized the contamination level by the *signal* in Spectral-SCR and the area of ROI 2 to compute normalized contamination levels.

To calculate the Projection-SCR, we used the mean value in ROI 1 and the mean value in ROI 2. The equation is as follows:

$$\text{Projection} - \text{SCR} = \frac{\text{mean}(\text{ROI1}) - \text{mean}(\text{ROI2})}{\text{mean}(\text{ROI2})} \tag{4}$$

These three quantities are used to quantify the quality of the experimentally acquired data at different activities of In-111 source and with/without the CDCP technique.

### F. Comparison With Triple Energy Window Scatter Correction

We compared the effect of CDCP with the traditional triple energy window (TEW) scatter correction [9] on 171 keV gamma-photons using the In-111 line source with Ac-225 contamination dataset. With TEW, we estimated the scattered

counts on each pixel on the imaging detector as

$$C_{scatter} = \left( \frac{C_{lower}}{w_{lower}} + \frac{C_{upper}}{w_{upper}} \right) \frac{w_{main}}{2}, \qquad (5)$$

where $C_{lower}$ and $C_{upper}$ are the total counts in the lower/upper energy windows with the widths of $w_{lower}/w_{upper}$. $w_{main}$ denotes the width of the primary energy window.

Therefore, the corrected count for each pixel is:

$$C_{corrected} = C_{raw} - C_{scatter}, \qquad (6)$$

where $C_{raw}$ denotes the total count in the primary energy window. In this study, since there were also other photopeaks around 171 keV emitted from Ac-225, we chose narrow lower and upper energy windows: [155 keV, 165 keV] and [176 keV, 186 keV], respectively.

Because of the low sensitivity of the prototype system, we acquired the raw data for a long time, i.e., 50 hours for the last angle. To demonstrate the super-low-activity imaging capability, we used the raw data to compare CDCP and TEW data corresponding to different acquisition times and sensitivities. Specifically, taking 171 keV as the primary gamma-photon, the coincidence count rate is proportional to the sensitivity of detecting 245 keV gamma-photons with coincidence detectors. The sensitivity of the prototype system to detect 245 keV gamma-photons is estimated to be 3%. Therefore, for example, we can have the same CDCP results with 50-hour acquisition and 3% sensitivity, or with 3-hour acquisition and 50% sensitivity which is possible to achieve in a future preclinical CDCP-SPECT. According to this equivalence, we can compare the effect of CDCP and TEW with different acquisition time only based on our acquired raw data.

### G. Image Reconstruction

From the pixelated projections at three angles, we reconstructed the image with the maximum-likelihood expectation-maximization (MLEM) algorithm [38].

$$f_l^{(t+1)} = \frac{f_l^{(t)}}{sen_l} \sum_{j=1}^{N} \frac{P_{jl} I_j}{\sum_{i=1}^{M} P_{ji} f_i^{(t)}}, \qquad (7)$$

where $\mathbf{f}$ is the source distribution, $f_i^{(t)}$ is the $t'$th iteration of the activity at source voxel $i$. The sensitivity $sen_l$ is the probability that a gamma-photon originated from source voxel $l$ is detected. $I_j$ is the intensity of detector voxel $j$ in the projection. $P_{jl}$ is the probability of a photon originating from source voxel $l$ being detected at detector voxel $j$, so-called system response function (SRF). To calculate SRF, we used a voxel-driven method [39] that we implemented in our previous studies [40], [41]. A geometrical calibration was carried out to calibrate the precise system geometry including the positions and orientations of the imaging detector, the pinhole collimator, and motors. In the model, we included the attenuation and DOI response of the detector, but Compton scattering was not modeled.

In this study, we reconstructed the images of 171 keV and 245 keV photopeaks from the In-111 line source

with/without Ac-225 background. Since different energies experience varying degrees of attenuation, we computed two separate SRFs for 171 keV and 245 keV, respectively.

### H. Evaluation of the Influence of the Coincidence Detectors' Energy Resolution

The energy resolution is an important capability to provide spectral information for coincidence. With a higher energy resolution and a narrower energy window, there will be fewer random coincidence events falling into the time gate. For imaging detectors, there is no doubt that detectors with high energy and spatial resolutions should be used. For coincidence detectors, considering the cost of high-resolution detectors, this evaluation is to study how poor of the energy resolution we can still accept without losing too much accuracy of coincidence.

To experimentally estimate the influence of the coincidence detectors' energy resolution on CDCP, we used the dataset acquired from the In-111 line source with Ac-225 background and blurred the energies measured by the coincidence detectors with artificial Gaussian blurring.

In this study, we take 171 keV as the primary gamma-photons and 245 keV as the secondary gamma-photons. With the energy spectra acquired from the coincidence detectors, we fitted the contamination around the 245 keV peak and used Gaussian fitting to fit the contamination-subtracted 245 keV peak to get the standard deviation $\sigma_2$. As described in Sec. II-B, any interactions with the energy deposition inside $245\text{keV} \pm 3\sigma_2$ energy window starts a time gate for coincidence.

To simulate detectors with various energy resolutions, we artificially added a Gaussian random number to every measured energy so that the resultant Gaussian-fitted FWHM of the contamination-subtracted 245 keV peak is the *target* value. The Gaussian random number yields a distribution of $N\left(0, \sigma_2'^2\right)$ where $\sigma_2'^2$ is fixed for different energies and only depends on the *target* FWHM value. To account for the low-cost and widely used scintillation detectors, we set the *target* FWHM value at 245 keV to be 5 keV, 10 keV, 20 keV, and *no energy resolution*. After blurring, the secondary energy window was also adjusted according to $245\text{keV} \pm 3\sigma_2$. Note that with *no energy resolution*, we consider all interactions on the coincidence detectors as the secondary gamma-photons ($\sigma_2$ is $+\infty$) to open time gates.

Finally, we compared the metrics as described in Sec. II-E as well as the reconstructed images to evaluate the effect of CDCP with different energy resolutions of coincidence detectors.

### I. Evaluation of the Influence of the Detector Timing Resolution, the Decay Time of the Cascade Emission, and the Width of the Time Gate

Like energy resolution, timing resolution also has an influence on CDCP, and the influence could be different for different decay constants of the cascade emissions. In addition, as mentioned in Sec. II-B, there is a trade-off between the number of true coincidence events and the proportion of true

coincidence when we select the time gate. In this study, with the Monte Carlo method, we simulated 100,000 pairs of cascade photons and different numbers of contamination photons using MATLAB [42] so that we could optimize the time gate with regard to different timing resolutions and different half-lives of cascade emissions.

Considering a radionuclide emitting $\gamma_1$ and $\gamma_2$ cascade photons with the half-life, $T_{1/2}$, of the intermediate energy level, we take $\gamma_1$ as the primary gamma-photon and $\gamma_2$ as the secondary gamma-photon. Some notations are as follows:

- Number of pairs of cascade photons per second: $A = 10^5 \text{ s}^{-1}$.
- The sensitivity of the imaging detector to detect $\gamma_1$:$s_1$.
- The sensitivity of the detection system to detect $\gamma_2$:$s_2$.
- Timing resolution (FWHM) of the detection system: $\Sigma$.
- Width of the time gate: $\tau$.
- **Detected** single count rate from non-primary gamma photons inside $\gamma_1$ energy window on the imaging detector: $N_1$.
- The probability of detecting the true cascade photon pairs inside the time gate: $P(\tau, T_{1/2}, \Sigma)$.
- The measured random coincidence count rate with CDCP: $R(N_1, s_2A, \tau)$,
- The measured scatter coincidence count rate with CDCP: $S$.

To simplify the problem, $R(N_1, s_2A, \tau)$ is considered to only depend on detected events inside $\gamma_1$ energy window induced by a) down scattering from **high-energy** gamma-photons or crosstalk on the imaging detector and b) the **secondary** gamma-photons, $\gamma_2$, detected by the whole system. There are three major reasons. *First*, in this simulation, $\gamma_1$ as the primary gamma-photon does not contribute to the final contamination. *Second*, we do not consider the Compton scattering of $\gamma_1$ or $\gamma_2$ given the low activity. *Third*, we ignored the random coincidence between both single down-scattered events with one inside $\gamma_1$ energy window on the imaging detector and the other inside $\gamma_2$ energy window by the whole system induced by two high-energy gamma-photons. Noting that the penetration problem for high-energy photons leads to the use of low energy gamma-photons for SPECT imaging, we assumed that $\gamma_1$ has lower energy than $\gamma_2$. Thus, for the whole system, the detected events with the energy deposition inside $\gamma_2$ energy windows are mainly from the photoelectric effect instead of down-scattering from high-energy gamma-photons.

To quantify the effect of various configurations, we used Noise Equivalent Count Rate (NECR), similar to it in PET [43], with the equation:

$$\text{NECR} = \frac{(True\ count\ rate)^2}{True\ count\ rate + Contamination\ count\ rate}, \quad (8)$$

where *True count rate* refers to true coincidence and *Contamination count rate* refers to random coincidence and scatter coincidence. Assuming that the count rates do not reach the dead time limit of the detectors and the half-lives of the primary and the background sources are much longer than the time gate, the expectation of the number of single contamination events inside the time gate opening by a $\gamma_2$ is

$N_1 \cdot \tau$. Note that given a time gate with a width of $\tau$, it starts before $\gamma_2$ and is optimized to have the most true coincidence events according to different timing resolutions and half-lives of the intermediate energy levels. As a result, the expectation of $R(N_1, s_2A, \tau)$ is $s_2AN_1\tau$.

Note that $A$ is the emission rate of cascade photons instead of the activity, $s_1$ and $s_2$ are affected by the energies of cascade photons and the system geometry. In this simulation, for simplification, $A, s_1, s_2$ were fixed to study the influence of $T_{1/2}, \Sigma, N_1$ on the selection of the time gate and the optimal NECR. Given the condition of $T_{1/2}, \Sigma, N_1$, the NECR with CDCP could be expressed as

$$\begin{aligned}
&\text{NECR}\left(\tau \mid T_{1/2}, \Sigma, N_1\right) \\
&= \frac{\left(s_1s_2AP\left(\tau, T_{1/2}, \Sigma\right)\right)^2}{\left(s_1s_2AP\left(\tau, T_{1/2}, \Sigma\right)\right) + R\left(N_1, s_2A, \tau\right) + S} \\
&= \frac{s_1s_2A\left(P\left(\tau, T_{1/2}, \Sigma\right)\right)^2}{P\left(\tau, T_{1/2}, \Sigma\right) + \frac{N_1\tau}{s_1} + \frac{S}{s_1s_2A}}.
\end{aligned} \quad (9)$$

In most of cases, scatter coincidence could be neglected, so NECR with CDCP could be written as

$$\begin{aligned}
\text{NECR}\left(\tau \mid T_{1/2}, \Sigma, N_1\right) &= \frac{s_1s_2A\left(P\left(\tau, T_{1/2}, \Sigma\right)\right)^2}{P\left(\tau, T_{1/2}, \Sigma\right) + \frac{N_1\tau}{s_1}} \\
&\propto \frac{A\left(P\left(\tau, T_{1/2}, \Sigma\right)\right)^2}{P\left(\tau, T_{1/2}, \Sigma\right) + \frac{N_1\tau}{s_1}}.
\end{aligned} \quad (10)$$

Similarly, the NECR without CDCP could be written as

$$\text{NECR}_{\text{single}} = \frac{(s_1A)^2}{s_1A + N_1}. \quad (11)$$

Hence, the enhancement of NECR with CDCP could be calculated by the ratio of Eq. (10) and (11)

$$\text{Enh\_NECR} = \frac{s_2\left(P\left(\tau, T_{1/2}, \Sigma\right)\right)^2\left(1 + \frac{N_1}{As_1}\right)}{P\left(\tau, T_{1/2}, \Sigma\right) + \frac{N_1}{s_1}\tau}. \quad (12)$$

To simulate $P(\tau, T_{1/2}, \Sigma)$, we generated $A$ pairs of timestamps during 1 second and made the time difference of each pair yield exponential distribution with the half-life of $T_{1/2}$. An artificial Gaussian blurring with the FWHM of $\Sigma$ was applied to all timestamps and the distribution of these blurred time differences was computed. $P(\tau, T_{1/2}, \Sigma)$ was the integration of the distribution of blurred time differences within the time gate. Note that given the width of the time gate, we optimized the starting point of the time gate by maximizing $P(\tau, T_{1/2}, \Sigma)$.

We set
- $T_{1/2}$ to 0.1 ns, 0.3 ns, 0.5 ns, 85 ns,
- $\Sigma$ from 0.1 ns to 500 ns,
- $N_1/s_1$ to $10^5 \text{ s}^{-1}, 10^6 \text{ s}^{-1}, 10^7 \text{ s}^{-1}$,

to study their influences on the optimal NECR, {$\text{NECR}\left(\tau \mid T_{1/2}, \Sigma, N_1\right)$}, and the optimal time gate, {$\text{NECR}\left(\tau \mid T_{1/2}, \Sigma, N_1\right)$}. Note that the half-lives we set followed the decay time of cascade emissions of Ac-225, Ra-223, Lu-177 and In-111. In addition, $As_1$ denotes the detected count rate of primary gamma-photons on the imaging detector, which is comparable to $N_1$. Hence, $N_1/s_1$ denotes

the equivalent contamination level in the object space which is comparable to $A$. Since it appears as a whole part in the equations, we changed it directly in our simulation.

### J. Estimation of the Effect of CDCP on Different Radionuclides

To estimate the effect of reducing down-scattered and crosstalk contamination and losing true signals with CDCP on different radionuclides, we first derive the theoretical signal-to-contamination ratio (Theoretical-SCR), which is defined as

$$\text{Theoretical} - \text{SCR} = \frac{True\ count\ rate}{Contamination\ count\ rate}. \quad (13)$$

Considering the notations in Sec. II-H, the enhancement of Theoretical-SCR can be expressed as

$$\text{Enh\_SCR} = \frac{\text{SCR}_{\text{CDCP}}}{\text{SCR}_{\text{single}}} = \frac{\frac{s_1 s_2 A P(\tau, T_{1/2}, \Sigma)}{N_1 s_2 A \tau + S}}{\frac{s_1 A}{N_1}}$$

$$= \frac{P(\tau, T_{1/2}, \Sigma)}{\tau A + \frac{S}{N_1 s_2}}. \quad (14)$$

Therefore, the enhancement of Theoretical-SCR is nearly inversely proportional to the width of time gate and the emission rate of cascade photons, considering that the number of scatter coincidence events is small. For a fast cascade emission like Ac-225 (106 ps) and a high timing resolution system, a narrow time gate would allow us to achieve a high Theoretical-SCR and NECR simultaneously.

Since the timing resolution and the sensitivity of the prototype CDCP-SPECT system are poor, we are not able to demonstrate the enhancement with Ac-225. As a preliminary demonstration, we carried out a Monte Carlo simulation study with GEANT4 [44]. The simulated CDCP-SPECT setup comprised a CZT imaging detector, a GAGG coincidence detector, and a 1mm D tungsten pinhole collimator. The size of the CZT detector is 3 cm × 3 cm × 1 cm. It offers an energy resolution of 1.5% FWHM, a spatial resolution of 0.5 cm FWHM in 3 dimensions and a timing resolution of 10 ns FWHM [37]. The pinhole collimator is 1.5 cm thick and positioned at a distance of 1.5 cm from the CZT detector. It is aligned with the central axis of the CZT detector. An Ac-225 line source, emitting 117 keV and 465 keV cascade photons, was positioned at a distance of 2.5 cm from the pinhole. The line source is a cylinder with a radius of 0.8 cm and a length of 2.8 cm. In addition, the line source is oriented parallel to the CZT detector. The sensitivity to detect primary 117 keV gamma-photons is 0.035%. The GAGG coincidence detector is a 3-cm-thick hollow box covering the source with an opening section in case of blocking gamma-photons. The coincidence detector could achieve a sensitivity of ∼61% to detect the secondary 465 keV photons. The timing resolution of the GAGG detector is 1 ns FWHM. The time gate is set to [−10 ns, 10 ns].

We performed a simulation using a 50 $\mu$Ci Ac-225 source with a 2-hour acquisition time. This was done to reduce statistical fluctuations and assess the impact of the CDCP technique on reducing down-scattered contamination while
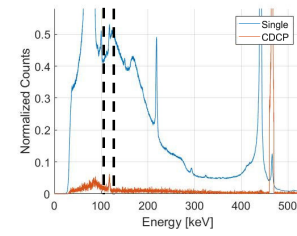


Fig. 7. Normalized energy spectra of Ac-225 acquired with the CZT detector module coupled with a pinhole collimator and processed without (blue) and with (red) the CDCP technique.
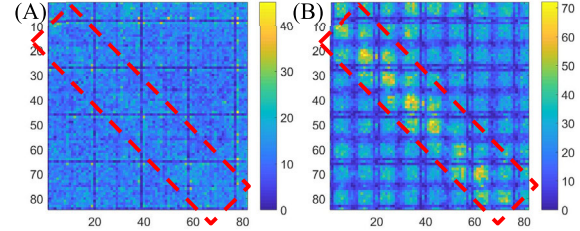


Fig. 8. Projections acquired from the 0.5 $\mu$Ci Ac-225 line source at: (A) 117 keV and (B) 218 keV. Red dashed boxes highlight the projected line source.

preserving true signals. Additionally, to demonstrate the projections for the super-low-activity scenario, we utilized a 0.5 $\mu$Ci Ac-225 line source with a 2-hour acquisition time. To generate the projection, we used 0.5 mm pixel pitch. This allowed us to visualize the effects of the CDCP technique on the resultant projections, considering the challenges associated with super-low-activity imaging conditions.

## III. RESULTS

### A. Experimental Demonstration of CDCP-Enhanced Data Acquisition Using the CZT-Based Prototype System

*1) Spectral Analysis With Ac-225:* Using the detector module coupled with the pinhole collimator, the normalized energy spectra acquired from Ac-225 without and with CDCP are shown in Fig. 7. The primary energy window [115 keV, 119 keV] is highlighted by the black dashed lines. The spectra were normalized by the net area of the 117 keV peaks. Noting that the detector module was not fully covered by the collimator but to have enough counts for Ac-225, we used the energy spectra on the whole module. After applying CDCP with a time gate of 500 ns and the $\gamma_2$ energy window of [460 keV, 470 keV], the down-scattered contamination around the 117 keV peak was dramatically reduced by ∼98%. Noting that we counted all interactions falling into the time gate started by $\gamma_2$ including $\gamma_2$, there is a high peak at 465 keV in the CDCP spectrum. The projection without CDCP at 117 keV and 218 keV are shown as Fig. 8. The red dashed boxes show the projected line source but for 117 keV gamma-photons, it is not visible because of down-scattered contamination. Due to the low activity and low sensitivity, we do not have enough data for CDCP processing. Hence, there is no further projection analysis.

*2) Spectral and Projection Analysis of In-111 Without Ac-225:* For the In-111 line source with/without Ac-225 background, the detector module was fully covered by the collimator. The energy resolutions are 2.4 keV and 3 keV FWHM at 171 keV
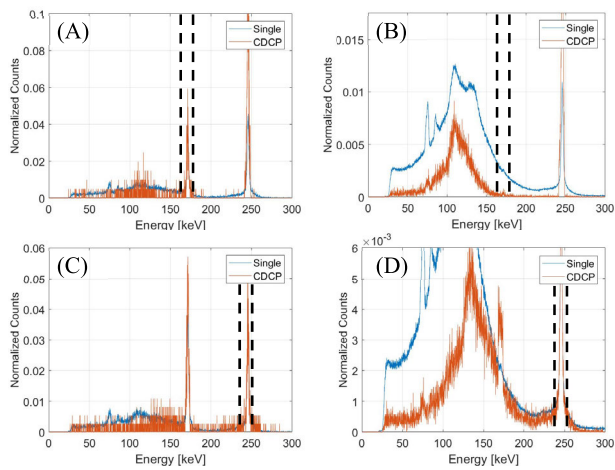
Fig. 9. Normalized energy spectra of In-111 without Ac-225 background in: (A) ROI 1 and (B) ROI 2, taking 171 keV as the primary energy; (C) ROI 1 and (D) ROI 2, taking 245 keV as the primary energy. The blue/red curves show spectra without /with the CDCP technique, respectively.
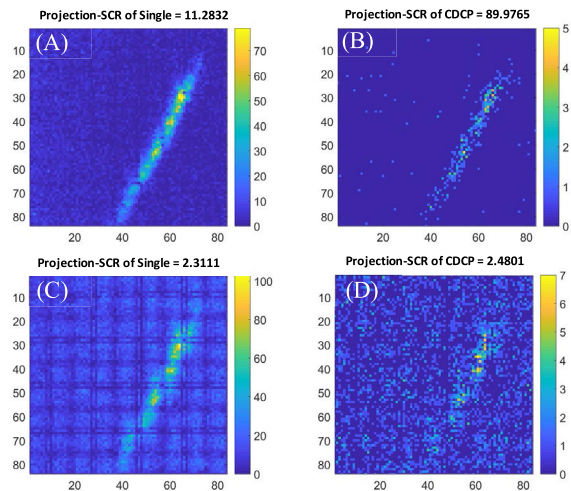


Fig. 10. Projections of the In-111 line source without Ac-225 background: (A) without CDCP, (B) with CDCP, taking 171 keV as the primary energy; (C) without CDCP, (D) with CDCP, taking 245 keV as the primary energy.

and 245 keV, respectively. Hence, the energy windows for 171 keV and 245 keV are [168.3 keV,174.3 keV] and [241 keV, 249 keV], respectively. To apply CDCP, we used a time gate of 500 ns.

Using the data acquired at the last angle's and an In-111 line source *without* Ac-225, the normalized energy spectra in ROI 1 and ROI 2 are shown in Fig. 9 (A)(B), taking 171 keV as the primary energy. The primary energy windows are shown with black dashed lines. With the metrics described in Sec. II-E, the Spectral-SCR with CDCP increases to 29.1 from 9.27 without CDCP. The normalized contamination level with CDCP was reduced to 0.01 from 0.1 without CDCP. Taking 245 keV as the primary energy, the normalized energy spectra in ROI 1 and ROI 2 are shown as Fig. 9 (C)(D). Since there is no scatter contamination at 245 keV, Spectral-SCRs without/with CDCP are both ~17, and normalized contamination levels are both ~0.27. Note that the spectra are normalized by the net area of the primary photopeak. The projections without/with CDCP taking 171 keV as the primary energy are shown in

Fig. 10 (A)(B). The Projection-SCR is improved from 11.3 to 90.0 with CDCP. Taking 245 keV as the primary energy, the projections without/with CDCP are shown in Fig. 10 (C)(D). Because of the same reason (no scattered contamination), the Projection-SCR is not improved. In addition, as shown in Fig. 9 (D) and Fig. 10 (C)(D), there is a penetration issue for 245 keV gamma-photons.
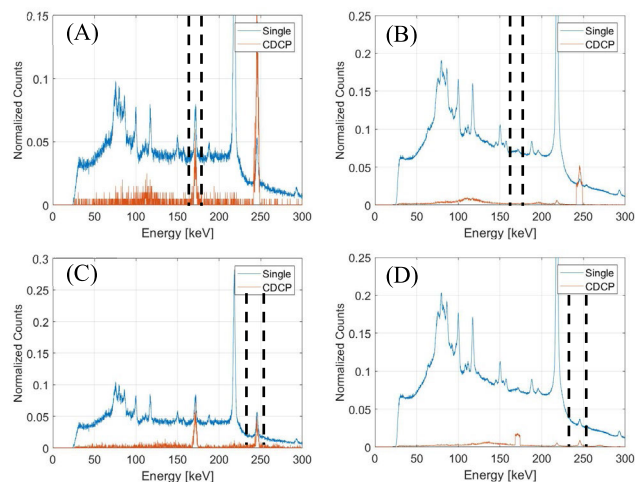


Fig. 11. Normalized energy spectra of In-111 with Ac-225 contamination in: (A) ROI 1 and (B) ROI 2, taking 171 keV as the primary energy; (C) ROI 1 and (D) ROI 2, taking 245 keV as the primary energy. The blue/red curves show spectra without /with the CDCP technique, respectively.

*3) Spectral and Projection Analysis of In-111 with Ac-225:* Using the last angle's data of the In-111 line source *with* Ac-225, the normalized energy spectra in ROI 1 and ROI 2 are shown as Fig. 11 (A)(B), taking 171 keV as the primary energy. The primary energy windows are shown with black dashed lines. The Spectral-SCRs with CDCP at 171 keV energy window are increased to 12.7 from 0.59 without CDCP. The normalized contamination levels at 171 keV energy window reduced to 0.07 from 3.29, which means CDCP could reduce ~98% of contamination in this setup. Taking 245 keV as the primary energy, as shown in Fig. 11 (C)(D), the Spectral-SCR is improved to 9.4 from 2.2 with CDCP, while the normalized contamination level is reduced to 0.28 from 1.95.

Taking 171 keV as the primary energy, the projections without/with CDCP are shown as Fig. 12 (A)(B). The Projection-SCR is improved from 0.31 to 15.9 with CDCP. Taking 245 keV as the primary energy, the projections without/with CDCP are shown as Fig. 12 (C)(D). The Projection-SCR is improved from 0.34 to 2.5 with CDCP. It is worth noting that taking 245 keV as the primary energy, the three metrics with the CDCP enhancement are improved to the same level as In-111 without Ac-225 (no contamination at 245 keV).

We summarized the Spectral-SCRs, normalized contamination (NC) levels, and the Projection-SCR at three angles as Table II, III, and IV. As mentioned in Sec. II-D at these three angles, the activities of the In-111 line source decayed from 0.7 $\mu$Ci to 0.35 $\mu$Ci. It is worth noting that the enhancement of Spectral-SCR and Projection-SCR, which
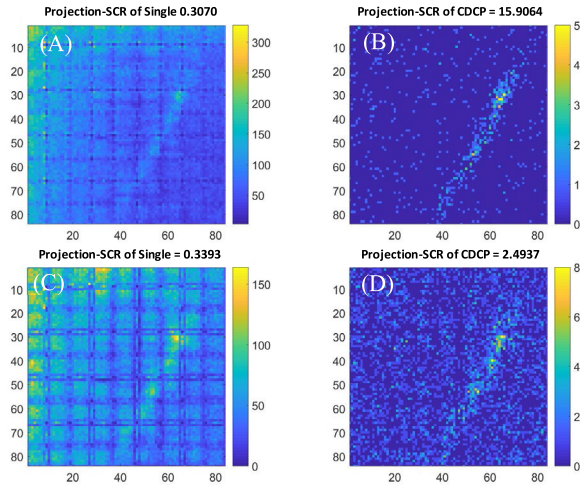
Fig. 12. Projections of the In-111 line source with Ac-225 background: (A) without CDCP, (B) with CDCP, taking 171 keV as the primary energy; (C) without CDCP, (D) with CDCP, taking 245 keV as the primary energy.

TABLE II
SPECTRAL-SCR WITH AND WITHOUT CDCP AT DIFFERENT
ACTIVITIES OF IN-111 AT 171 KEV

| Activities of In-111 | 0.7 µCi | 0.55 µCi | 0.35 µCi |
|---|---|---|---|
| Spectral-SCR of Single | 1.28 | 0.98 | 0.58 |
| Spectral-SCR of CDCP | 12.21 | 10.76 | 12.67 |
| Enhancement | 9.53 | 10.96 | 21.52 |

is the ratio between the quantities with and without CDCP, as well as the reduction of normalized contamination, defined as $\frac{NC(single)-NC(CDCP)}{NC(single)}$, increases as the activity of In-111 decreases.

## B. Comparison of TEW-Corrected and CDCP-Enhanced Data at Different Acquisition Time

Taking 171 keV as the primary energy, the TEW-corrected projections of the In-111 line source with Ac-225 background at the last angle are shown in Fig. 13. With decreasing acquisition time from 50 hours to 3 hours, the Projection-SCRs of TEW-corrected projections are also decreasing from 3.87 to 1.00.

The CDCP-enhanced projection shown in Fig. 12(B) ($s_2 = 3\%$, 50-hour acquisition) shows much better Projection-SCR of 15.91. This CDCP-enhanced projection is also equivalent to being acquired with a higher sensitivity system and shorter acquisition time: ($s_2 = 10\%$, 15-hour acquisition), ($s_2 = 20\%$, 7.5-hour acquisition) or ($s_2 = 50\%$, 3-hour acquisition). These high sensitivities are achievable in a preclinical CDCP-SPECT system with large coverage of high stopping power coincidence detectors. Clearly, the effect of TEW is worse than CDCP.

## C. Experimental Evaluation of the Influence of the Coincidence Detectors' Energy Resolution

In this study, we merged the three angles of data acquired from the In-111 line source with Ac-225 background for spectral analysis. Taking 171 keV as the primary energy, the
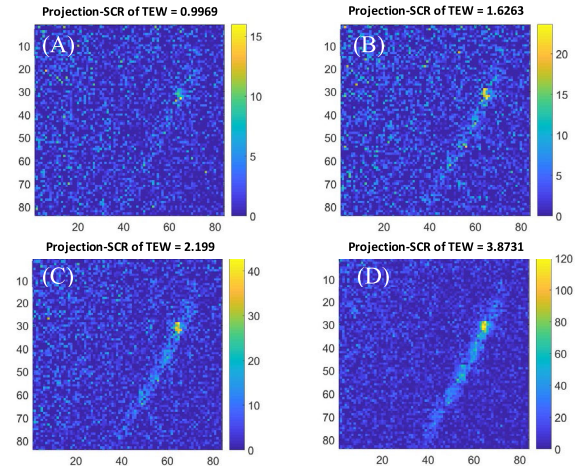


Fig. 13. TEW-corrected Projections of the In-111 line source with Ac-225 background of: (A) 3-hour acquisition, (B) 7.5-hour acquisition, (C) 15-hour acquisition, and (D) 50-hour acquisition.
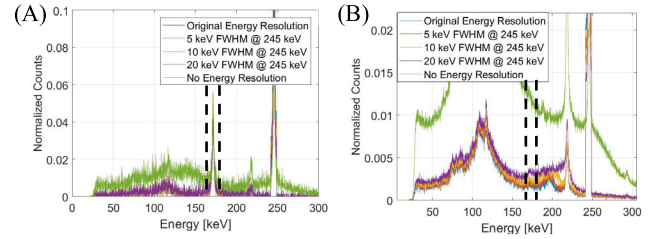


Fig. 14. Energy spectra of In-111 source with Ac-225 background with the CDCP technique: (A) in ROI 1, (B) in ROI 2. In the processing of CDCP, the energy resolutions of three coincidence detectors at 245 keV were artificially blurred to: no blurring, 5 keV FWHM, 10 keV FWHM, 20 keV FWHM, and no resolution.

TABLE III
NORMALIZED CONTAMINATION (NC) WITH AND WITHOUT
CDCP AT DIFFERENT ACTIVITIES OF IN-111 AT 171 KEV

| Activities of In-111 | 0.7 µCi | 0.55 µCi | 0.35 µCi |
|---|---|---|---|
| NC of Single | 1.65 | 2.02 | 3.29 |
| NC of CDCP | 0.086 | 0.076 | 0.07 |
| Reduction | 94.7% | 96.2% | 97.9% |

TABLE IV
PROJECTION-SCR WITH AND WITHOUT CDCP AT DIFFERENT
ACTIVITIES OF IN-111 AT 171 KEV

| Activities of In-111 | 0.7 µCi | 0.55 µCi | 0.35 µCi |
|---|---|---|---|
| Projection-SCR of Single | 0.62 | 0.39 | 0.30 |
| Projection-SCR of CDCP | 15.61 | 13.48 | 15.9 |
| Enhancement | 25.2 | 34.6 | 53 |

resultant energy spectra with/without CDCP in ROI 1 and ROI 2 are shown as Fig. 14. The primary energy windows are shown with black dashed lines. We applied the artificial energy blurring on the coincidence detectors described in Sec. II-H. Even though we merged three angles of data, the low measured counts still lead to the relatively high statistical fluctuation in ROI 1, which makes it hard to distinguish the spectra with different blurring in Fig. 14(A). As shown in Fig. 14(B), with worse energy resolutions, the effect of reducing NB becomes worse.

TABLE V
SPECTRAL-SCR AND NC WITH DIFFERENT DATASETS AT DIFFERENT
ENERGY RESOLUTIONS OF COINCIDENCE DETECTORS

| Energy Resolution at 245 keV of Coincidence Detectors | Original | 5 keV FWHM | 10 keV FWHM | 20 keV FWHM | No Resolution |
|---|---|---|---|---|---|
| Spectral-SCR merging three angles | 11.77 | 10.91 | 9.67 | 8.12 | 2.63 |
| NC merging three angles | 0.08 | 0.09 | 0.11 | 0.15 | 0.57 |

TABLE VI
PROJECTION-SCR AT DIFFERENT ENERGY RESOLUTIONS OF
COINCIDENCE DETECTORS AND AT DIFFERENT ACTIVITIES OF IN-111

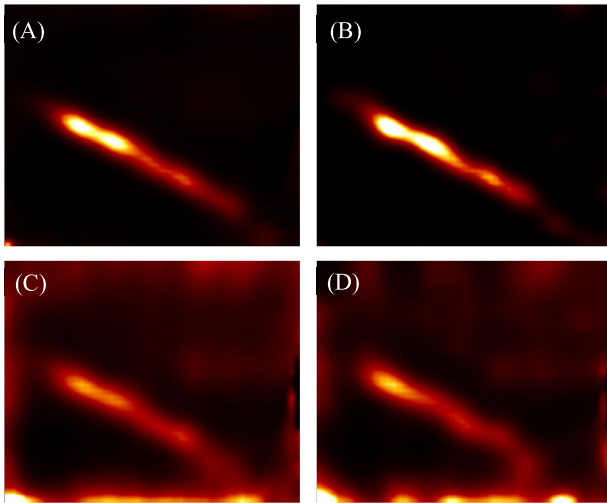| Energy Resolution at 245 keV of Coincidence Detectors | Original | 5 keV FWHM | 10 keV FWHM | 20 keV FWHM | No Resolution |
|---|---|---|---|---|---|
| Projection-SCR at 0.7 µCi | 15.61 | 14.11 | 12.36 | 9.64 | 2.64 |
| Projection-SCR at 0.55 µCi | 13.49 | 12.32 | 10.40 | 7.77 | 2.11 |
| Projection-SCR at 0.35 µCi | 15.90 | 13.68 | 10.63 | 6.89 | 1.71 |



Fig. 15. Reconstructed images of the In-111 line source without Ac-225 background: (A) 171 keV without CDCP, (B) 171 keV with CDCP, (C) 245 keV without CDCP, (D) 245 keV with CDCP.

Quantitative comparisons were conducted with the metrics as described in Sec. II-E. We summarized the Spectral-SCRs and NBs at different energy resolutions as Table V. Note that after we merged the datasets, in a single 171 energy window, the Spectral-SCR without CDCP is 0.87 while the NB without CDCP is 2.15. Projection-SCRs at three different angles (activities) and different energy blurring are summarized in Table VI.

## D. Preliminary Imaging Study of CDCP-SPECT

To evaluate the enhancement of the CDCP technique on the resultant images, we carried out imaging studies using the In-111 line source without/with Ac-225 background. In this study, the object space has $48 \times 40 \times 40$ cubic voxels of 0.5 mm $\times$ 0.5 mm $\times$ 0.5 mm in size. All shown images are the $15^{th}$ iteration.

In the absence of Ac-225 background and without the CDCP enhancement, the reconstructed images of 171 keV and 245 keV are shown in Fig. 15(A)(C). With the CDCP
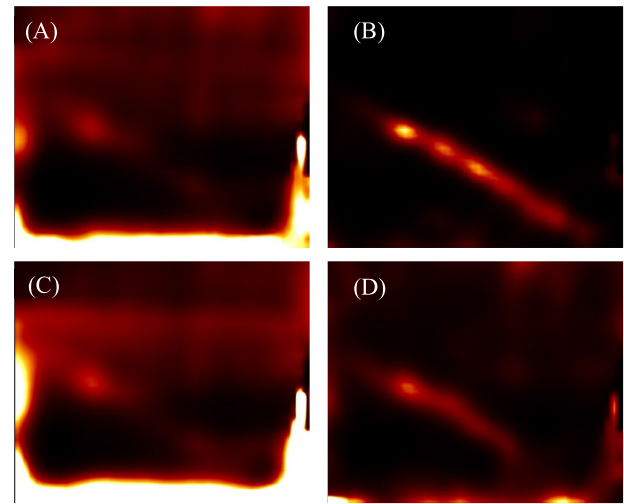


Fig. 16. Reconstructed images of the In-111 line source with Ac-225 background: (A) 171 keV without CDCP, (B) 171 keV with CDCP, (C) 245 keV without CDCP, (D) 245 keV with CDCP.
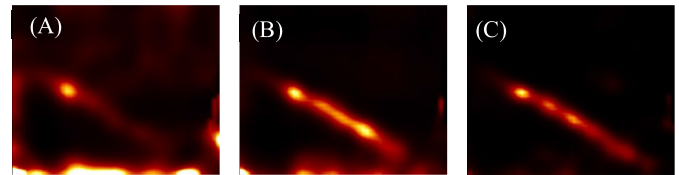


Fig. 17. Reconstructed images of the In-111 line source with Ac-225 background: (A) 171 keV with TEW (6-hour acquisition), (B) 171 keV with TEW (106-hour acquisition), (C) 171 keV with CDCP (6-hour acquisition, $s_2 = 50\%$ or 106-hour acquisition, $s_2 = 3\%$).

enhancement, the reconstructed images of 171 keV and 245 keV are shown in Fig. 15(B)(D). No visible difference is observed between the images obtained without the CDCP enhancement and those with the CDCP enhancement.

In the presence of Ac-225 background, the conventional reconstructed images of 171 keV and 245 keV are shown as Fig. 16 (A)(C). The enhancement is significant. Due to the excessive down-scattered contamination contribution from the Ac-225 source, the In-111 line source cannot be recognized with the regular pinhole data acquisition. After applying CDCP, the reconstructed images shown in Fig. 16(B)(D) are significantly enhanced.

Images reconstructed with TEW correction and CDCP enhanced are compared in Fig. 17. Artifacts around the line source in Fig. 17(A)(B) are introduced by down-scattering contamination. It is evident from the comparison that the CDCP technique exhibits superior performance compared to TEW correction, particularly in low-activity scenarios.

The TEW-corrected reconstructed images with varying acquisition times (ranging from 6 hours to 106 hours) are shown in Fig. 18.

After artificial Gaussian blurring, the CDCP-enhanced reconstructed images with varying energy resolutions (ranging from 5 keV to 20 keV FWHM and no resolution) of coincidence detectors are shown in Fig. 19. This is reasonable according to the Projection-SCRs of the experimentally acquired projections as summarized in Table. VI.
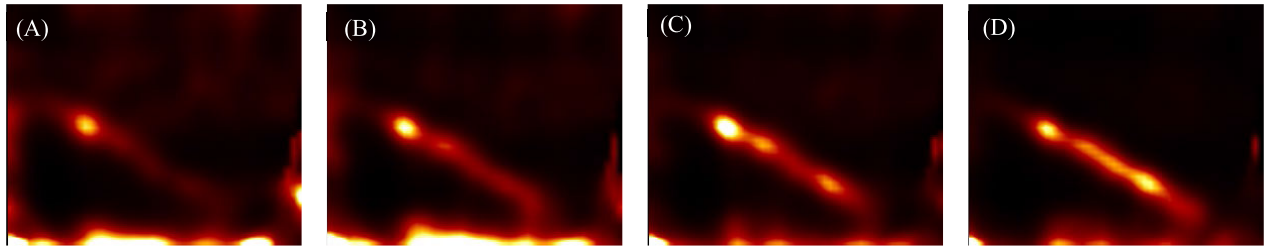
Fig. 18. Reconstructed images with TEW correction for different acquisition time: (A) 6-hour acquisition, (B) 16-hour acquisition, (C) 32-hour acquisition, (D) 106-hour acquisition in total (three angles).
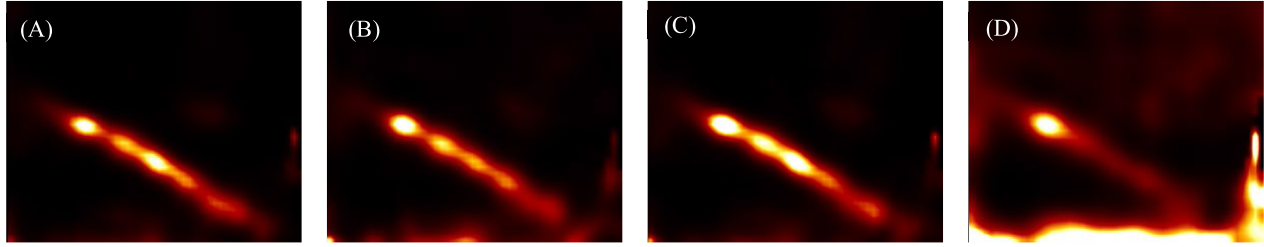


Fig. 19. Reconstructed images with CDCP applying different energy resolutions at 245 keV of the coincidence detectors: (A) 5 keV FWHM, (B) 10 keV FWHM, (C) 20 keV FWHM, (D) no energy resolution.

## E. Experimental Evaluation of the Influence of Timing Resolution, Decay Time of the Cascade Gamma-Photon Emission, and the Width of the Time Gate

As we described in Sec. II-I, the optimal time gate and optimal NECR were simulated for the half-lives of the intermediated energy level of 0.1 ns, 0.2 ns, 0.5 ns, and 85 ns which are related to some useful cascade photons emitted by Ac-225, Ra-223, Lu-177 and In-111.

The optimal time gates at different contamination levels and at different time resolutions are shown as Fig. 20-22 (A). To compare the change of optimal NECR of different radionuclides as the timing resolution chances in the same scale, we plotted the normalized optimal NECR at different contamination levels as Fig. 20-22 (B). The maxima of NECR, expressed in counts per second (cps), for various radionuclides and at different levels of contamination, are summarized in Table VII. When the coincidence timing resolution is better than 10 ns, there is no difference among Ac-225, Ra-223, and Lu-177. For a system with $< 10$ ns timing resolution, the optimal time gates are shorter with higher contamination levels.

## F. Estimation of the Effect of CDCP on Other Radionuclides

As we described in Sec. II-J, we carried out a Monte Carlo simulation study with GEANT4 to assess the efficacy of the CDCP technique for Ac-225. In the 50 $\mu$Ci Ac-225 simulation, we acquired 154,751 interactions inside the primary [114.3 keV, 120.3 keV] energy window, and 41% of them were from 117 keV emissions. With the time gate of [−10 ns, 10 ns] and the secondary [445 keV, 485 keV] energy window, we have 36,874 interactions still inside the primary energy window, and 99.5% of them are from 117 keV emissions. In the remaining 200 (0.5%) coincidence events, half of them are random coincidence events and the others are
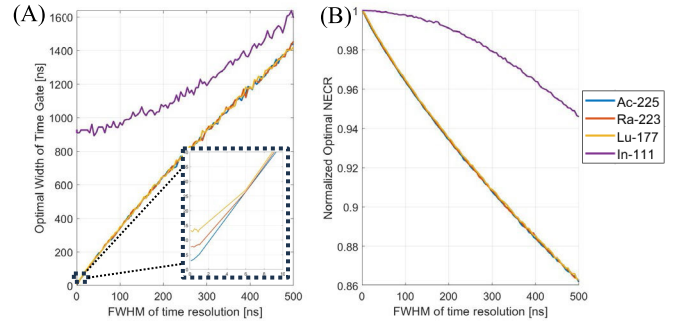


Fig. 20. (A) Optimal time gate vs. time resolution and (B) normalized optimal NECR vs. time resolution for Ac-225, Ra-223, Lu-177 and In-111. $N_1/s_1 = 10^5$ s$^{-1}$.



Fig. 21. (A) Optimal time gate vs. time resolution and (B) normalized optimal NECR vs. time resolution for Ac-225, Ra-223, Lu-177 and In-111. $N_1/s_1 = 10^6$ s$^{-1}$.

scatter coincidence events. To sum up, the CDCP technique could reject ∼99.8% of scattered and crosstalk gamma-photons. However, ∼39% of true 117 keV gamma-photons were rejected at the same time because their cascade 465 keV gamma-photons were not detected. As a result, Theoretical-SCR is improved by ∼300 times, and NECR is improved by ∼1.4 times for 117 keV energy window.
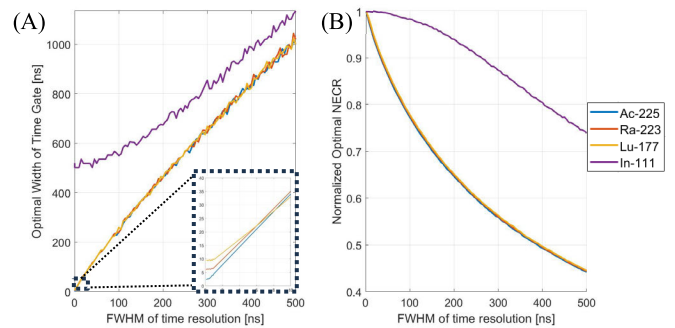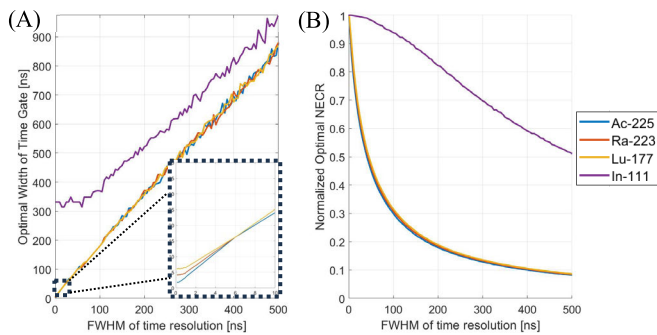
Fig. 22. (A) Optimal time gate vs. time resolution and (B) normalized optimal NECR vs. time resolution for Ac-225, Ra-223, Lu-177 and In-111. $N_1/s_1 = 10^7 \text{ s}^{-1}$.

TABLE VII

MAXIMA OF NECR WITH DIFFERENT RADIONUCLIDES AT DIFFERENT CONTAMINATION LEVELS

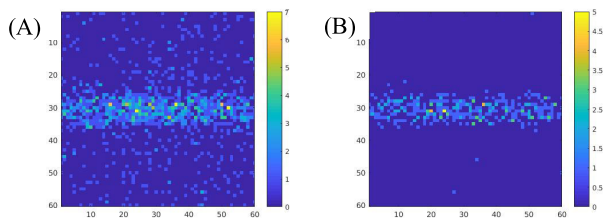| $N_1/s_1$ | Ac-225 | Ra-223 | Lu-177 | In-111 |
|---|---|---|---|---|
| $10^5 \text{s}^{-1}$ | $10.0 \times 10^4$ | $9.99 \times 10^4$ | $9.98 \times 10^4$ | $8.94 \times 10^4$ |
| $10^6 \text{s}^{-1}$ | $9.97 \times 10^4$ | $9.93 \times 10^4$ | $9.89 \times 10^4$ | $5.59 \times 10^4$ |
| $10^7 \text{s}^{-1}$ | $9.81 \times 10^4$ | $9.52 \times 10^4$ | $9.29 \times 10^4$ | $1.41 \times 10^4$ |



Fig. 23. Simulated projections from Ac-225 at 117 keV: (A) without CDCP, (B) with CDCP.

If we applied [−50 ns, 50 ns] time gate, 38,128 interactions were kept and 98.33% of them are true from 117 keV emission. In the remaining 636 coincidence events, ∼500 events are random coincidences. This is proportional to the time gate as derived. The others are scatter coincidences which is the same as the time gate of [−10 ns, 10 ns].

The projections acquired from the 0.5 $\mu$Ci Ac-225 line source without/with CDCP are shown in Fig. 23. Note that since the simulation setup is highly simplified, the down-scattered contamination could be underestimated in Fig.23(A).

## IV. DISCUSSION

In SPECT imaging, it is common for sources to emit gamma-photons with multiple energies. This can occur in various applications, such as in RPT and simultaneous multi-isotope imaging. In such cases, non-primary gamma photons can contribute to the photopeak of primary gamma photons through scattering and crosstalk effects. This can lead to significant contamination in the resulting SPECT images. We proposed and experimentally evaluated CDCP-SPECT imaging in this study, which allows us to fundamentally reduce the scattered and crosstalk contamination. This technique utilizes cascade photons and both of them can be treated as the primary gamma-photon while considering the other as the secondary gamma-photon. The time gates for these two cases are different, which should be optimized as described in Sec. II-I.

Since our prototype system has poor timing resolution and bad sensitivity, we were not able to acquire projection and imaging studies to demonstrate the CDCP enhancement with Ac-225 experimentally. Consequently, we used an experimental "simulation" approach, combining In-111 and Ac-225 to simulate the detection of Tl-209 cascade photons with the presence of down scattered contamination from higher-energy gamma-photons from Ac-225 and its daughters. Since In-111 emitting 171 keV and 245 keV cascade photons, our prototype system has a much higher sensitivity (3%) for detecting the 245 keV gamma-photons. Through our experiments, we demonstrated that the CDCP technique significantly improved several metrics:

1) In the spectral domain, Spectral-SCR was improved approximately 22 times, indicating better differentiation between target signals and scattered/crosstalk contamination. Note that this is in the region where the object is directly projected through the collimator.
2) In the spectral domain, the normalized contamination was reduced by approximately 98%, indicating a substantial reduction of scattered/crosstalk contamination in the region where the object cannot be projected through the collimator.
3) In the projection domain, the Projection-SCR was improved approximately 53 times, highlighting the increased visibility and clarity of the target features.

Compared to a traditional scatter correction method, achieving a reasonable Projection-SCR in the projection domain using the TEW correction method requires a 50-hour acquisition time. However, using the CDCP technique, we were able to achieve a much higher Projection-SCR even with a significantly shorter acquisition time of 3 hours ($s_2 = 50\%$). Furthermore, when comparing the resultant images, it was observed that the TEW-corrected images exhibited higher levels of contamination than those enhanced with the CDCP technique. This indicates that the CDCP approach effectively reduces contamination and improves image quality, providing clearer and more precise details in the resulting images. Additionally, it is important to note that the efficacy of the TEW correction method is influenced by the number of counts obtained within the energy windows. With less acquisition time, the number of counts is reduced, which can decrease the efficacy of the TEW correction, resulting in lower image quality and compromised Projection-SCR. Using In-111 with Ac-225 background demonstrates the potential use of CDCP in low-activity preclinical imaging for radionuclides emitting cascade photons. However, there needs to be a direct representation of the complexities and challenges involved in imaging therapeutic radionuclides in preclinical applications.

It is worth noting that in the projection domain, as the In-111 line source decays over time, the enhancement of Spectral-SCR and Projection-SCR becomes more prominent. This can be explained with Eq. (14) in Sec. II-J. The remaining contamination after applying the CDCP technique primarily arises from random coincidences, and the count rate of random coincidences is proportional to the rate of cascade emission, as assumed in Sec. II-I. Therefore, Theoretical-SCR with CDCP remains relatively constant, assuming that the detected count rate from non-primary gamma-photons ($N_1$)

remains unchanged, while the SCR without CDCP decreases as the activity decreases. Similarly, metrics in this study, Spectral-SCR, and Projection-SCR follow the same trend as Theoretical-SCR. In addition, the random coincidence rate is also proportional to the count rate of down-scattering gamma-photons from high-energy photons and the width of time gate. When using a single radionuclide independently like In-111, the down-scattering contamination from its 245 keV emissions is not significantly high, resulting in fewer random coincidences. However, when one employs Ac-225 as the sole radionuclide, there is a much higher proportion of these high-energy photons. This can lead to an increased number of down-scattering gamma-photons, subsequently elevating the potential for random coincidences. Fortunately, systems with high timing resolutions can effectively reduce the incidence of these random coincidences by adjusting the time gate appropriately.

Crucially, as derived in Eq. (13) and (14), the efficacy of CDCP showcases a near-inverse proportionality to the cascade emission rate. This relationship underscores CDCP's heightened effectiveness, particularly in low-activity scenarios. The rationale behind this is the disproportionate increase in random coincidence events compared to true coincidence events as the activity decreases. For traditional scatter correction methods, their performance tends to diminish as activities are reduced. Significantly, the methodology behind our CDCP technique does not conflict with conventional methods. In scenarios involving standard-activity imaging, a synergistic approach integrating both could be adopted, potentially yielding enhanced imaging outcomes.

According to Eq. (12) and Eq. (14), a more dramatic improvement of Theoretical-SCR and NECR could be potentially achieved with radionuclides having fast cascade emissions, such as Ac-225, and using a high timing resolution system. This is because a shorter time gate can be utilized to simultaneously achieve a high probability of detecting cascade photons, $P\left(\tau, T_{1/2}, \Sigma\right)$, and low random coincidence count rate. In our simulation study, we utilized a reasonably high-time-resolution system which allowed us to use a shorter time gate (4% of that for In-111) for Ac-225. As a result, an enhancement of Theoretical-SCR for $\sim$300 times was achieved. Note that the down-scattered contamination could be underestimated in this highly simplified simulation setup, which suggests that the enhancement of NECR could potentially be even higher than the reported value of 1.5 in the simulation study. In Ac-225 targeted-$\alpha$-therapy, the use of 218 keV and 440 keV gamma-photons emitted from the daughters of Ac-225 (Fr-221 and Bi-213) for localization presents challenges in terms of collimation due to their high penetration. As we mentioned in Sec. II. A, despite the relatively low branch ratio (1.5%) for Ac-225 to emit 117 keV gamma-photons, the measured count rate is still comparable to that of 218 keV and 440 keV gamma-photons considering the detection efficiency for different energies. Without the implementation of CDCP, imaging the 117 keV gamma-photons becomes exceedingly challenging due to the significant scatter and crosstalk contamination. However, with the application of CDCP, it becomes possible

to effectively eliminate the contamination at the 117 keV photopeak. Additionally, the short half-life of Tl-209, which is approximately 2.2 minutes, offers the potential for a similar distribution as that of Bi-213. This characteristic enhances the feasibility and relevance of imaging Tl-209, as its distribution can serve as an indicator for the distribution of Bi-213. This underscores the crucial role of CDCP in enabling the imaging of the 117 keV gamma-photons emitted by Ac-225 (Tl-209/Bi-213) and addresses the penetration problem encountered with higher energy photons.

With artificial energy blurring, we evaluated the influence of energy resolutions of coincidence detectors on CDCP enhancement by comparing the three quantities as mentioned in Sec. II-E. The results showed that the enhancement of CDCP was similar if the energy resolution of the coincidence detectors is better than 10 keV FWHM at 245 keV.

With Monte Carlo simulation, we estimated the influence of the time gate and timing resolution of the system with different half-lives of the cascade emissions using NECR as a reference. The results showed that the optimal NECR is higher with a better timing resolution system and a faster decayed intermediated energy level, which follows our expectations. As the equivalent contamination level increases, the increase of NECR becomes more significant with a better timing resolution, and a shorter time gate is needed at the same time. Note that in our simulation, we used pre-set equivalent contamination levels, $N_1/s_1$. However, in practice, it needs to be determined from Theoretical-SCR inside the primary energy window of the imaging detector. The Theoretical-SCR is equivalent to $As_1/N_1$, then $N_1/s_1$ could be computed for post-processing with knowing $A$. In addition, according to Eq. (12), the enhancement of NECR is also linearly influenced by $s_2$ the sensitivity of the detection system to detect the secondary gamma-photon. This relationship arises from the acceptance criteria of primary gamma-photons: they are only considered if the secondary gamma-photon is also detected. Therefore, in spite of almost eliminating contamination, a proportion $(1 - s_2)$ of true signals (primary gamma-photon) are discarded. In this study, $s_2$ of the prototype system is low, considering the geometry and detector material. As we look to the future, with large-volume high-stopping-power scintillation materials coupled with large solid angle coverage, we could curtail the loss of true signals and achieve a high NECR. However, a crucial problem remains: achieving extensive solid angle coverage, especially beyond 50%, poses challenges in a clinical setting. Given this limitation, our technique aligns more fittingly with preclinical imaging systems.

It is worth noting that the use of a simple phantom as well as the artificial sources (In-111 with Ac-225 background) during experiments provides a baseline for evaluating the technique's performance. However, there are reservations about how well the technique will perform with more complex phantoms in practical preclinical settings. To address these potential challenges, a CDCP-SPECT with high timing resolution and high sensitivity should be constructed. In addition, further studies and experiments should be conducted using more realistic and complex phantoms that better mimic the heterogeneous nature of biological tissues. This will help

assess the technique's performance in various preclinical scenarios and provide insights into its limitations and potential improvements.

## V. CONCLUSION

In therapeutic radionuclide SPECT imaging, even if the administered activity is high, the radioactive uptake within the tissues of interest can be notably low. This results in limited measured counts, which can undermine the efficacy of traditional scatter correction methods. To address this challenge, our study introduces the CDCP technique, designed specifically to effectively eliminate down-scattered and crosstalk contamination in scenarios with low activity. We experimentally evaluated the CDCP-SPECT for imaging low-activity radionuclides through a prototype CDCP-SPECT system. It is experimentally demonstrated that with the In-111 line source in the presence of Ac-225 background, the technique allows us to improve the Spectral-SCR for ∼20 times and the Projection-SCR for ∼53 times and reduce ∼98% of the normalized contamination. Compared with the TEW scatter correction method, which only enhances the Projection-SCR to 1.00, the CDCP technique stands out by boosting the Projection-SCR to 15.91. This comparison has demonstrated CDCP's superior capability to mitigate down-scattered contamination, a feature that becomes even more pronounced at lower activity levels. The reconstructed images also showcase the dramatic enhancement of the image quality with CDCP-SPECT compared to the conventional and TEW-corrected SPECT.

We also used artificial energy blurring and Monte Carlo simulation to evaluate the influence of energy and timing resolutions on CDCP. The results could give us a great clue to constructing a preclinical or small animal CDCP-SPECT system. The GEANT4 simulation study shows the potential of improving the Theoretical-SCR for ∼300 times and reducing ∼99.8% of scattered contamination with Ac-225, an important therapeutic radionuclide. These dramatically reduced down-scattered and crosstalk contamination, coupled with the outstanding energy resolution offered by the CZT detectors, allow for a dramatically improved Theoretical-SCR and NECR for imaging low-activity therapeutic radionuclides, such as Ac-225, Ra-223, Lu-177, and In-111.

## ACKNOWLEDGMENT

## REFERENCES

[1] A. Morgenstern, C. Apostolidis, C. Kratochwil, M. Sathekge, L. Krolicki, and F. Bruchertseifer, "An overview of targeted alpha therapy with $^{225}$Actinium and $^{213}$Bismuth," *Current Radiopharmaceuticals*, vol. 11, no. 3, pp. 200–208, Oct. 2018.

[2] C. Parker et al., "Targeted alpha therapy, an emerging class of cancer agents," *JAMA Oncol.*, vol. 4, no. 12, p. 1765, Dec. 2018.

[3] P. Thakral et al., "Dosimetric analysis of patients with gastro entero pancreatic neuroendocrine tumors (NETs) treated with PRCRT (peptide receptor chemo radionuclide therapy) using Lu-177 DOTATATE and capecitabine/temozolomide (CAP/TEM)," *Brit. J. Radiol.*, vol. 91, no. 1091, Nov. 2018, Art. no. 20170172.

[4] E. Lazzeri, P. Erba, M. Perri, R. Doria, C. Tascini, and G. Mariani, "Clinical impact of SPECT/CT with In-111 biotin on the management of patients with suspected spine infection," *Clin. Nucl. Med.*, vol. 35, no. 1, pp. 12–17, 2010.

[5] P. Prior et al., "A modified TEW approach to scatter correction for In-111 and Tc-99m dual-isotope small-animal SPECT," *Med. Phys.*, vol. 43, no. 10, p. 5503, Oct. 2016.

[6] S. Ben-Haim et al., "Simultaneous dual-radionuclide myocardial perfusion imaging with a solid-state dedicated cardiac camera," *Eur. J. Nucl. Med. Mol. Imag.*, vol. 37, no. 9, pp. 1710–1721, Aug. 2010.

[7] J. Maffey-Steffan et al., "The $^{68}$Ga/$^{177}$Lu-theragnostic concept in PSMA-targeting of metastatic castration-resistant prostate cancer: Impact of post-therapeutic whole-body scintigraphy in the follow-up," *Eur. J. Nucl. Med. Mol. Imag.*, vol. 47, no. 3, pp. 695–712, Mar. 2020.

[8] R. J. Jaszczak, K. L. Greer, C. E. Floyd Jr., C. C. Harris, and R. E. Coleman, "Improved SPECT quantification using compensation for scattered photons," *J. Nucl. Med., Off. Publication, Soc. Nucl. Med.*, vol. 25, no. 8, pp. 893–900, 1984.

[9] V. Changizi, A. Takavar, A. Babakhani, and M. Sohrabi, "Scatter correction for heart SPECT images using TEW method," *J. Appl. Clin. Med. Phys.*, vol. 9, no. 3, pp. 136–140, Jun. 2008.

[10] K. Ogawa, Y. Harata, T. Ichihara, A. Kubo, and S. Hashimoto, "A practical method for position-dependent Compton-scatter correction in single photon emission CT," *IEEE Trans. Med. Imag.*, vol. 10, no. 3, pp. 408–412, Mar. 1991.

[11] T. Ichihara, K. Ogawa, N. Motomura, A. Kubo, and S. Hashimoto, "Compton scatter compensation using the triple-energy window method for single- and dual-isotope SPECT," *J. Nucl. Med.*, vol. 34, no. 12, pp. 2216–2221, Dec. 1993.

[12] H. Vija, M. S. Kaplan, and D. R. Haynor, "Simultaneous estimation of SPECT activity and attenuation distributions from measured phantom data using a differential attenuation method," in *Proc. IEEE Nucl. Sci. Symp., Conf. Rec., Nucl. Sci. Symp. Med. Imag. Conf.*, Oct. 1999, pp. 884–888.

[13] S. Hapdey, M. Soret, and I. Buvat, "Quantification in simultaneous $^{99m}$Tc/$^{123}$I brain SPECT using generalized spectral factor analysis: A Monte Carlo study," *Phys. Med. Biol.*, vol. 51, no. 23, pp. 6157–6171, Dec. 2006.

[14] J. Buvat, H. Benali, F. Frouin, J. P. Basin, and R. D. Paola, "Target apex-seeking in factor analysis of medical image sequences," *Phys. Med. Biol.*, vol. 38, no. 1, pp. 123–137, Jan. 1993.

[15] M. Asl, A. Sadremomtaz, and A. Bitarafan-Rajabi, "Evaluation of six scatter correction methods based on spectral analysis in $^{99m}$Tc SPECT imaging using SIMIND Monte Carlo simulation," *J. Med. Phys.*, vol. 38, no. 4, p. 189, 2013.

[16] K. Knešaurek and J. Machac, "Enhanced cross-talk correction technique for simultaneous dual-isotope imaging: A TL-201/Tc-99m myocardial perfusion SPECT dog study," *Med. Phys.*, vol. 24, no. 12, pp. 1914–1923, Dec. 1997.

[17] E. C. Frey, K. L. Gilland, and B. M. W. Tsui, "Application of task-based measures of image quality to optimization and evaluation of three-dimensional reconstruction-based compensation methods in myocardial perfusion SPECT," *IEEE Trans. Med. Imag.*, vol. 21, no. 9, pp. 1040–1050, Sep. 2002.

[18] I. Laurette, G. L. Zeng, A. Welch, P. E. Christian, and G. T. Gullberg, "A three-dimensional ray-driven attenuation, scatter and geometric response correction technique for SPECT in inhomogeneous media," *Phys. Med. Biol.*, vol. 45, no. 11, pp. 3459–3480, Nov. 2000.

[19] S. C. Moore, J. Ouyang, M.-A. Park, and G. El Fakhri, "Monte Carlo-based compensation for patient scatter, detector scatter, and crosstalk contamination in in-111 SPECT imaging," *Nucl. Instrum. Methods Phys. Res. A, Accel. Spectrom. Detect. Assoc. Equip.*, vol. 569, no. 2, pp. 472–476, Dec. 2006.

[20] T. C. D. Wit et al., "Hybrid scatter correction applied to quantitative holmium-166 SPECT," *Phys. Med. Biol.*, vol. 51, no. 19, pp. 4773–4787, Oct. 2006.

[21] P. Fan et al., "Scatter and crosstalk corrections for $^{99m}$Tc/$^{123}$I dual-radionuclide imaging using a CZT SPECT system with pin-hole collimators," *Med. Phys.*, vol. 42, no. 12, pp. 6895–6911, Dec. 2015.

[22] T. Bexelius and A. Sohlberg, "Implementation of GPU accelerated SPECT reconstruction with Monte Carlo-based scatter correction," *Ann. Nucl. Med.*, vol. 32, no. 5, pp. 337–347, Jun. 2018.

[23] H. Xiang, H. Lim, J. A. Fessler, and Y. K. Dewaraja, "A deep neural network for fast and accurate scatter estimation in quantitative SPECT/CT under challenging scatter conditions," *Eur. J. Nucl. Med. Mol. Imag.*, vol. 47, no. 13, pp. 2956–2967, Dec. 2020.

[24] J. Bai, J. Hashimoto, K. Ogawa, T. Nakahara, T. Suzuki, and A. Kubo, "Scatter correction based on an artificial neural network for $^{99m}$Tc and $^{123}$I dual-isotope SPECT in myocardial and brain imaging," *Ann. Nucl. Med.*, vol. 21, no. 1, pp. 25–32, Jan. 2007.

[25] P. K. Leichner et al., "Patient-specific dosimetry of indium-111-and yttrium-90-labeled monoclonal antibody CC49," *J. Nucl. Med.*, vol. 38, no. 4, pp. 512–516, 1997.

[26] P. Kletting, T. Kull, S. N. Reske, and G. Glatting, "Comparing time activity curves using the Akaike information criterion," *Phys. Med. Biol.*, vol. 54, no. 21, pp. N501–N507, Nov. 2009.

[27] J. Caravaca, Y. Huh, G. T. Gullberg, and Y. Seo, "Compton and proximity imaging of AC in vivo with a CZT gamma camera: A proof of principle with simulations," *IEEE Trans. Radiat. Plasma Med. Sci.*, vol. 6, no. 8, pp. 904–915, Nov. 2022.

[28] B. F. Hutton, I. Buvat, and F. J. Beekman, "Review and current status of SPECT scatter correction," *Phys. Med. Biol.*, vol. 56, no. 14, pp. R85–R112, Jul. 2011.

[29] X. Liu et al., "A 3-dimensional stationary cascade gamma-ray coincidence imager," *Phys. Med. Biol.*, vol. 66, no. 22, Nov. 2021, Art. no. 225001.

[30] M. Uenomachi, K. Shimazoe, K. Ogane, and H. Takahashi, "Simultaneous multi-nuclide imaging via double-photon coincidence method with parallel hole collimators," *Sci. Rep.*, vol. 11, no. 1, Jun. 2021, Art. no. 13330, doi: 10.1038/s41598-021-92583-4.

[31] K. Shimazoe, M. Uenomachi, and H. Takahashi, "Imaging and sensing of pH and chemical state with nuclear-spin-correlated cascade gamma rays via radioactive tracer," *Commun. Phys.*, vol. 5, no. 1, p. 24, Jan. 2022.

[32] Y. Zhu, S. E. Anderson, and Z. He, "Sub-pixel position sensing for pixelated, 3-D position sensitive, wide band-gap, semiconductor, gamma-ray detectors," *IEEE Trans. Nucl. Sci.*, vol. 58, no. 3, pp. 1400–1409, Jun. 2011.

[33] Z. He, W. Li, G. F. Knoll, D. K. Wehe, J. Berry, and C. M. Stahle, "3-D position sensitive CdZnTe gamma-ray spectrometers," *Nucl. Instrum. Methods Phys. Res. A, Accel. Spectrom. Detect. Assoc. Equip.*, vol. 422, nos. 1–3, pp. 173–178, Feb. 1999.

[34] W. Li, Z. He, G. F. Knoll, D. K. Wehe, and Y. F. Du, "A modeling method to calibrate the interaction depth in 3-D position sensitive CdZnTe gamma-ray spectrometers," *IEEE Trans. Nucl. Sci.*, vol. 47, no. 3, pp. 890–894, Jun. 2000.

[35] F. Zhang, Z. He, D. Xu, G. F. Knoll, D. K. Wehe, and J. E. Berry, "Improved resolution for 3-D position sensitive CdZnTe spectrometers," *IEEE Trans. Nucl. Sci.*, vol. 51, no. 5, pp. 2427–2431, Oct. 2004.

[36] L. J. Meng and Z. He, "Estimate interaction timing in a large volume HgI detector using cathode pulse waveforms," *Nucl. Instrum. Methods Phys. Res. A, Accel. Spectrom. Detect. Assoc. Equip.*, vol. 545, nos. 1–2, pp. 234–251, Jun. 2005.

[37] L. J. Meng and Z. He, "Exploring the limiting timing resolution for large volume CZT detectors with waveform analysis," *Nucl. Instrum. Methods Phys. Res. A, Accel. Spectrom. Detect. Assoc. Equip.*, vol. 550, nos. 1–2, pp. 435–445, Sep. 2005.

[38] L. Parra and H. H. Barrett, "List-mode likelihood: EM algorithm and image quality estimation demonstrated on 2-D PET," *IEEE Trans. Med. Imag.*, vol. 17, no. 2, pp. 228–235, Apr. 1998.

[39] E. C. Frey and B. M. W. Tsui, "Collimator-detector response compensation in SPECT," in *Quantitative Analysis in Nuclear Medicine Imaging*. Boston, MA, USA: Springer, 2006, pp. 141–166.

[40] X. Lai and L.-J. Meng, "Simulation study of the second-generation MR-compatible SPECT system based on the inverted compound-eye gamma camera design," *Phys. Med. Biol.*, vol. 63, no. 4, Feb. 2018, Art. no. 045008.

[41] X. Lai, E. M. Zannoni, J. George, and L.-J. Meng, "System modeling and evaluation of a prototype inverted-compound eye gamma camera for the second generation MR compatible SPECT," *Nucl. Instrum. Methods Phys. Res. A, Accel. Spectrom. Detect. Assoc. Equip.*, vol. 954, Feb. 2020, Art. no. 162046.

[42] *Version 0.3.0.713579 (R2017b)*, MathWorks Inc, Natick, MA, USA, 2017.

[43] M. A. Queiroz, S. D. Wollenweber, G. von Schulthess, G. Delso, and P. Veit-Haibach, "Clinical image quality perception and its relation to NECR measurements in PET," *EJNMMI Phys.*, vol. 1, no. 1, p. 103, Dec. 2014.

[44] S. Agostinelli, "GEANT4—A simulation toolkit," *Nucl. Instrum. Methods Phys. Res. A, Accel. Spectrom. Detect. Assoc. Equip.*, vol. 506, no. 3, pp. 250–303, 2003.